Characterizing Near-Surface Moisture Increase during the Clear-Sky Afternoon-to-Evening Transition Using a Single-Column Model

SIWEI HE,[a] JULIA M. SIMONSON,[b,c,d] DAVID D. TURNER,[b] STANLEY G. BENJAMIN,[b,c] AND JOSEPH B. OLSON[b]

[a] *Civil Engineering Department, Montana State University, Bozeman, Montana*
[b] *NOAA/Global Systems Laboratory, Boulder, Colorado*
[c] *Cooperative Institute for Research in Environmental Sciences, University of Colorado Boulder, Boulder, Colorado*
[d] *Developmental Testbed Center, Boulder, Colorado*

(Manuscript received 10 July 2024, in final form 27 February 2025, accepted 14 March 2025)

ABSTRACT: The afternoon-to-evening transition is the period when the atmospheric boundary layer transitions from convective to stable conditions. One noticeable feature during this transition period is the rapid increase in water vapor concentration near the surface. However, the mechanism behind the increase in water vapor remains poorly understood. This study investigated the processes contributing to the water vapor increase and the impacts of the land cover and horizontal advection on the water vapor increase using a single-column model for the clear-sky condition. Numerical experiments were conducted on three cases at the Atmospheric Radiation Measurement (ARM) Southern Great Plains (SGP) site. Evapotranspiration was found to be the main moisture source to the water vapor increase, and that change of the near-surface vertical temperature gradient from negative to positive is the trigger for this increase during the afternoon-to-evening transition. This is because the near-surface turbulence divergence term decreases due to the change in the buoyancy profile caused by vertical temperature gradient change. The impact of horizontal advection on water vapor varies, and it can either lead to an increase or a decrease in water vapor, depending on the spatial horizontal water vapor gradient. This study also found that land cover can influence the timing of the water vapor increase since different land covers may have different Bowen ratios. Water vapor increases earlier under conditions with smaller Bowen ratios compared to those with larger values.

SIGNIFICANCE STATEMENT: This study investigates the processes that lead to the increase in near-surface water vapor during the afternoon-to-evening transition, a well-observed phenomenon. We employ a single-column model to simulate land–atmosphere interactions during this transition. It shows that evapotranspiration is the main contributor to the water vapor increase during the transition and that the change of the near-surface vertical temperature gradient from negative to positive is the trigger for this increase. Furthermore, this study reveals that horizontal advection can either lead to an increase or a decrease in water vapor during the transition, depending on the spatial horizontal water vapor gradient. These findings are consistent with in situ observations, as water vapor increases are typically recorded more frequently in summer than in winter, aligning with the magnitude of evapotranspiration.

KEYWORDS: Boundary layer; Atmosphere-land interaction; Numerical analysis/modeling

1. Introduction

Land–atmosphere (LA) interactions play an important role in weather and climate prediction since they are a main driver of Earth's surface water and energy budgets (Santanello et al. 2018). The atmospheric boundary layer (ABL) is the part of the atmosphere that is directly influenced by its contact with Earth's surface and responds to surface forcing with a time scale of about an hour or less (Stull 1988). Generally, surface heating by the Sun results in a thermally unstable and well-mixed convective boundary layer (CBL), and surface cooling results in a thermally stable boundary layer (SBL). In this way, the ABL experiences transitions from stable to unstable/convective states in the morning (i.e., morning transition) and from unstable/convective to stable states in the late afternoon or early evening (hereafter called the evening transition) (Angevine et al. 2020). Of course, the exact state of the ABL is the result of complex two-way interactions between local processes such as surface fluxes and entrainment at the ABL top as well as large-scale and mesoscale processes such as advection and subsidence.

Among others, morning and evening transitions are two features of the ABL that are not well studied and present challenges that are different from the fully stable and fully convective states (i.e., Grant 1997; Angevine et al. 2020). However, the structure and evolution of the ABL during transitions are still important in many practical applications, such as in predicting the possibility of fog or frost. Different from the well-developed ABL states, all of the forcings are weak during those transition periods. These forcings change in magnitude quickly, and few simplifications are possible to neglect them. For example, as the Sun sets, the incoming shortwave radiation decreases to zero, with the other terms of the LA system responding on different time scales, and their magnitudes change differently throughout this transition period. This affects the intensity of the turbulent mixing in the ABL, which often develops a more complicated structure through the evening transition (Acevedo and Fitzjarrald 2001).

One noticeable feature with the evening transition is the relatively sudden increase in the near-surface moisture

Corresponding author: Siwei He, siwei.he@montana.edu

DOI: 10.1175/JAMC-D-24-0101.1

© 2025 American Meteorological Society. This published article is licensed under the terms of the default AMS reuse license. For information regarding reuse of this content and general copyright information, consult the AMS Copyright Policy (www.ametsoc.org/PUBSReuseLicenses).

Brought to you by NOAA Library | Unauthenticated | Downloaded 07/18/25 03:22 PM UTC

(e.g., Wingo and Knupp 2015; Blumberg et al. 2019). There are three associated hypotheses on the sudden moisture increase: 1) the moisture increase is due to evapotranspiration from the surface, as the latent heat flux often remains positive for an hour or more after the sensible heat flux goes negative around sunset; 2) the moisture is due to water vapor advection, as wind direction can shift around sunset in conditions with weak synoptic forcing; and 3) the moisture is transported from higher in the CBL toward the surface through turbulence (e.g., Wingo and Knupp 2015; Mahrt 2017; Blumberg et al. 2019).

A number of studies aiming at understanding the evening transition and variations of the atmospheric processes at work during these transitions are already available. Grant (1997) showed the presence of strong vertically curved profiles of sensible-heat and momentum fluxes that are initially restricted to a 400-m-thick layer adjacent to the surface. Acevedo and Fitzjarrald (2001) proposed that the evening transition is dominated by vertical flux convergence as the turbulent mixing layer becomes confined to a shallow stable layer near the surface, and using large-eddy simulations, they showed that the specific humidity jump during this period is primarily the consequence of the enhanced vertical flux divergence. Using observations from several sites across the Hudson Valley region within New York State, Acevedo and Fitzjarrald (2001) also showed that the impact of the surface heterogeneity is enhanced during the evening transition. Blumberg et al. (2019) analyzed 20 years of Oklahoma Mesonet data and found that a presunset near-surface water vapor maximum is strongly dependent on the spatial differences in evapotranspiration and the resulting advection (i.e., secondary circulation) caused by these spatial differences in land cover. Darbieu et al. (2015) investigated the vertical decay of ABL turbulence and change of vertical wind speed spectral shape in the afternoon transition using observations and large-eddy simulations (LESs). They showed that changes in these two variables start at the top of the boundary layer, meaning that the top of the boundary layer is affected by the surface change first. Using observations of 140 cases in Alabama, Wingo and Knupp (2015) also showed that horizontal wind variance and temperature monotonically decrease as surface heating diminishes, and water vapor increase begins about 80 min before sunset. Blay-Carreras et al. (2014) showed that a time delay exists between the time when the buoyancy flux ceases and the change in sign of the vertical gradient of the virtual potential temperature during the evening transition. Edwards et al. (2006) simulated the evening transition using a single-column model (SCM). They showed that the stability function in calculating diffusivities of momentum strongly impacted the performance of the model: When the stability function is sharp tailed, turbulent diffusion is systematically underestimated in the surface layer, while it is overestimated at greater heights.

However, these studies do not explicitly give an explanation for the near-surface water vapor increase. It is necessary to test the associated hypotheses on the sudden moisture increase in a systematic way to determine if one of the processes is dominant or if the dominant process varies over time. Accompanying the water vapor increase, there is frequently a rapid drop in surface temperature and a decay of wind speed (Acevedo and Fitzjarrald 2001). Also, impacts of land surface properties on the evening transition have not been demonstrated in these previous studies. Land surface properties play important roles in the evolution of the ABL (e.g., Mahrt 2000; van Heerwaarden et al. 2014; Blumberg et al. 2019). It is necessary to investigate the impacts of land surface properties on the evening transition.

In this study, a single-column model is used to simulate and investigate the evening transition over the Atmospheric Radiation Measurement (ARM) Southern Great Plains site in Oklahoma. The main purpose of this study is to 1) show the variations of humidity, wind, temperature, and near-surface variables during the evening transition; 2) illustrate the contributions of three moisture sources mentioned above on the rapid near-surface water vapor concentration increase during the evening transition; and 3) investigate the impact of the land cover and horizontal advection during evening transition periods.

2. Study domain and data

a. Study domain

This study focuses on the central facility (site C1, which is collocated with site E13) of the ARM Southern Great Plains (SGP) site (Sisterson et al. 2016). That region has been identified as one of the regions with the strong land–atmosphere coupling (Koster et al. 2004). The SGP atmospheric observatory was the first field measurement site established by the ARM program (Turner and Ellingson 2016). The SGP observatory consists of in situ and remote sensing instrument clusters (e.g., Sisterson et al. 2016; Yang et al. 2006). Unique aspects at the SGP observatory are the multiple locations where temperature, humidity, wind, and turbulence profiles are observed, as well as both collocated and distributed surface energy budget stations. The central facility (i.e., E13), located near Lamont in north-central Oklahoma, houses the core instrumentation for the SGP site and is the center of operations for SGP experiments.

This study predefines a 10 km × 10 km domain with the E13 in the center to conduct our simulations. The primary land cover of the domain is cropland, and the soil is dominated by silt loam.

b. Data

1) Vertical atmospheric profiles

Vertical profiles of temperature and water vapor are retrieved from observations made by the Atmospheric Emitted Radiance Interferometer (AERI) (https://doi.org/10.5439/1483830), which measures spectral downwelling infrared radiance between 3 and 19 μm with higher than 1 wavenumber resolution every 30 s (Knuteson et al. 2004). The Tropospheric Remotely Observed Profiling via Optimal Estimation (TROPoe) algorithm (Turner and Löhnert 2014; Turner and Blumberg 2019) uses an iterative Gauss–Newton approach to retrieve thermodynamic profiles from the observed radiances and other data sources (e.g., microwave radiometer brightness temperature, surface meteorology). In this study, we use these retrieved thermodynamic profiles to

Brought to you by NOAA Library | Unauthenticated | Downloaded 07/18/25 03:22 PM UTC

evaluate and validate the model's performance for various experiments. We limit our study to within 500 m from the ground since the thermodynamic information content in the AERI observations is highest near the surface and decreases with altitude (Turner and Löhnert 2021). In the lowest 500 m above the surface, the root-mean-square of AERI retrieval for temperature is usually below 0.8°C for temperature and below 0.4 g kg^{-1} for water vapor mixing ratio (Turner and Löhnert 2021).

Wind profiles at the central facility are measured using a Doppler lidar (DL; Pearson et al. 2009) (https://doi.org/10.5439/1178582). The DL operates in the near infrared and is sensitive to backscatter from atmospheric aerosol, which are assumed to be ideal tracers of atmospheric wind fields. The DL is capable of measuring radial velocities under clear-sky conditions with very good precision (typically ~10 cm s^{-1}). Due to the choice of scanning modes used by the ARM program, the time resolution of the DL horizontal wind speed data is about 10 min.

2) SURFACE STATIONS

Many surface observations are available at the central facility through different stations. In this study, we use latent and sensible heat flux measurements of the eddy covariance (ECOR) station (https://doi.org/10.5439/1097546), ground heat flux of the Energy Balance Bowen Ratio station (EBBR; https://doi.org/10.5439/1023895), surface radiation components of the quality control Solar Infrared Radiation station (https://doi.org/10.5439/1227214), 2-m air temperature and water vapor mixing ratio, and 10-m wind speed of the surface meteorology station (https://doi.org/10.5439/1025220).

3) INITIAL AND FORCING DATA

The NOAA Rapid Refresh (RAP) analysis data (https://registry.opendata.aws/noaa-rap/) are downloaded and extracted to provide initial and forcing data for the single-column model. The RAP model is a NOAA operational numerical weather forecast model with 13-km grid spacing that is initialized hourly by assimilating numerous operational data streams (although none from the SGP site). Details on the RAP model and its observations assimilated can be found in Benjamin et al. (2016). The forcing data from RAP are its hourly analysis data. In preparing the forcing data, the zonal and meridional wind profiles to nudge toward were taken directly from the RAP output, while the geostrophic wind was calculated from the outputted pressure and Coriolis force. In the calculations, the outputted pressure was first interpolated to a common height, and then the zonal and meridional gradients were calculated using seven RAP grid cells on either side of the center point with the center difference method. Large-scale vertical wind and pressure vertical velocities were calculated using the average of three RAP grid cells on either side of the center point. Potential temperature and water vapor mixing ratio were also nudged using profiles taken directly from the RAP output. The large-scale tendencies of potential temperature and water vapor mixing ratio due to horizontal advection were calculated using seven RAP grid cells on either side of the center point with the center difference method, while the tendencies of potential temperature and water vapor mixing ratio due to vertical advection were set to zero. The required initial soil variables to run the Rapid Update Cycle (RUC) LSM were also obtained directly from the RAP output, and a list of variables that need to be initialized is provided in the online supplement.

3. Model

a. SCM

The Common Community Physics Package (CCPP) SCM (Bernardet et al. 2024; Firl et al. 2022) is used in this study. The CCPP is part of the Unified Forecast System (UFS) (https://ufscommunity.org/), which is a community-based, coupled, comprehensive Earth modeling system. It is designed to be the source system for operational numerical prediction applications that produce forecast guidance used by NOAA. The CCPP SCM (https://github.com/NCAR/ccpp-scm) is a valuable tool for diagnosing the performance of physics and schemes, and it is also a lightweight tool for investigating surface–atmospheric interactions.

b. Model physics

Different physics suites are supported by the CCPP SCM. In this study, CCPP SCM, version 5.1.0 (https://github.com/NCAR/ccpp-scm/tree/v5.1.0), and SCM_HRRR suite, which contains the parameterizations used in the NOAA operational RAP and High-Resolution Rapid Refresh (HRRR) models (https://rapidrefresh.noaa.gov/hrrr/), are used. A brief list of the parameterizations in SCM_HRRR includes subgrid-scale cloud interstitial, Rapid Radiative Transfer Model for global climate model (RRTMG) radiation scheme (Iacono et al. 2008), Mellor–Yamada–Nakanishi–Niino (MYNN) surface layer scheme (Olson et al. 2021), RUC land surface model (Smirnova et al. 2016; He et al. 2021; Smirnova and Benjamin 2025), MYNN eddy-diffusivity/mass-flux (EDMF) boundary layer and shallow cloud scheme (Olson et al. 2019), Global Systems Laboratory (GSL) drag suite scheme (Kim and Doyle 2005; Toy et al. 2025), Global Forecast System (GFS) ozone photochemistry scheme (McCormack et al. 2006), GFS stratospheric H2O scheme (McCormack et al. 2008), and Thompson aerosol-aware cloud microphysics scheme (Thompson and Eidhammer 2014). Dowell et al. (2022) provide a full description of the HRRR model and its physical parameterizations.

c. Model parameters

In the simulation, the majority of parameters use the default values used in the operational HRRR model run by the National Weather Service. However, the leaf area index (LAI; e.g., Fang et al. 2019) was adjusted to better represent the characteristics of the study domain. The default value is read from a vegetation table based on the vegetation of the study domain; in the HRRR system, the primary land use around the E13 site is cropland. In reality, the land cover of the study domain is winter wheat, and the LAI from the general cropland in the vegetation table is higher than the LAI of the winter wheat. Thus, we obtained our LAI value from the Moderate Resolution Imaging Spectroradiometer (MODIS)

Brought to you by NOAA Library | Unauthenticated | Downloaded 07/18/25 03:22 PM UTC

TABLE 1. A list of parameters in configuring the CCPP SCM.

Parameter	Value	Physical meaning
thermo_forcing_type	2	An integer representing how forcing for temperature and moisture state variables is applied.
mom_forcing_type	3	An integer representing how forcing for horizontal momentum state variables is applied.
C_RES	96	An integer representing the grid size of the UFS atmosphere initial conditions.
spinup_timesteps	1200	The number of time steps to spinup.
relax_time	7200	A number representing the time scale in seconds for the relaxation forcing.
sfc_flux_spec	FALSE	If surface fluxes are specified from the forcing data or not.
sfc_type	1	An integer representing the character of the surface.
lsm_ics	TRUE	If LSM initial conditions are included.
do_spinup	TRUE	If allow the model to spin up before the "official" model integration starts.
reference_profile_choice	2	An integer representing the choice of reference profile to use above the supplied initialization and forcing data.
column_area	1.0×10^8	A value representing the characteristic horizontal domain area of the atmospheric column in square meters, analogous to the horizontal grid size of a 3D model.

data (MCD15A3H). In our simulations, this reduced the LAI from 4.0 to 2.5. Table 1 is a list of other values in configuring the CCPP SCM.

d. Moisture balance

The atmospheric moisture budget equation can be written as (e.g., Stull 1988)

$$\frac{\partial \overline{q}}{\partial t} + \overline{U_j}\frac{\partial \overline{q}}{\partial x_j} = \frac{S_q}{\overline{\rho_{\text{air}}}} - \frac{\partial \overline{u_j' q'}}{\partial x_j}, \tag{1}$$

where the first term represents the total change of the atmospheric water vapor over time, the second term represents advection of atmospheric water by mean wind, the third term represents the net body source/sink term (e.g., from precipitation and evapotranspiration), and the fourth term represents turbulent flux divergence/convergence. In the SCM, the advection term is provided by the forcing data. Note that we have explicitly restricted our analysis to cases with clear skies, thereby simplifying the analysis.

Since we are interested in the near-surface water vapor increase during the evening transition, the focus of this study is the lowest atmospheric model layer. Taking the lowest atmospheric model layer as a study object, the turbulent mixing term in Eq. (1) consists of two terms: one is associated with moisture flux from the surface into this layer due to evapotranspiration [i.e., $\overline{u_j' q_0'} = LH/(L_v \rho_w)$], and the other one is associated with moisture flux at the interface between the lowest model layer and the layer above (i.e., $\overline{u_j' q_1'}$). Assuming horizontal homogeneity, the turbulent mixing term can be written as

$$\frac{\partial \overline{u_j' q'}}{\partial x_j} \approx \frac{\partial \overline{w' q'}}{\partial z} \approx \left(\frac{\overline{w' q_1'} - \overline{w' q_0'}}{\Delta z}\right) = \frac{\overline{w' q_1'}}{\Delta z} - \frac{\overline{w' q_0'}}{\Delta z} = \frac{\overline{w' q_1'}}{\Delta z} - \frac{\frac{LH}{L_v \rho_w}}{\Delta z}, \tag{2}$$

where w is the vertical wind speed, q is the water vapor mixing ratio, LH is the latent heat flux, ρ_w is the density of water, L_v is the latent heat of vaporization for water, and Δz is the thickness of the lowest atmospheric model layer. A simplified scheme illustrating the moisture-related processes involved in the lowest atmospheric model layer is shown in Fig. 1. In this layer, the horizontal advection term is specified from the forcing data. The turbulent term is named as the planetary boundary layer (PBL) term in the SCM. To split contributions of these two terms indicated in Eq. (2), we can subtract the evapotranspiration term from the PBL term, and the residual should be the contribution from the layer above.

4. Case selection

In this study, 3 days in May 2019 were selected (13, 15, 16 May). These are clear-sky days selected to avoid uncertainties from the clouds and precipitation in studying the evening transition. The required initial conditions of the RUC LSM were also provided from the RAP forcing dataset, so the CCPP SCM is able to run with the fully functional RUC LSM; namely, the SCM was run with the two-way interactions between land surface and atmospheric processes at every time step. For each case, the model was initialized at 1200 UTC and was run for 24 h.

5. Results

a. Atmospheric profiles

Figure 2 shows the evolution of profiles of temperature, water vapor, and wind speed from the observations (i.e., AERI and DL instruments) and SCM above the SGP central facility. From the observed profiles of the three cases, it can be seen that the water vapor increases near and above the surface before sunset (which is marked with a vertical dashed line) in all three cases. At the same time, stable boundary layer development is starting even before sunset, with temperature cooler in the near-surface layer than above. Wind speed profiles also show that low-level jets, which are common phenomena in the study domain (e.g., Berg et al. 2015), started to form before sunset.

Comparing with the observed profiles, it can be seen that the simulated air temperature and water vapor profiles are

Brought to you by NOAA Library | Unauthenticated | Downloaded 07/18/25 03:22 PM UTC

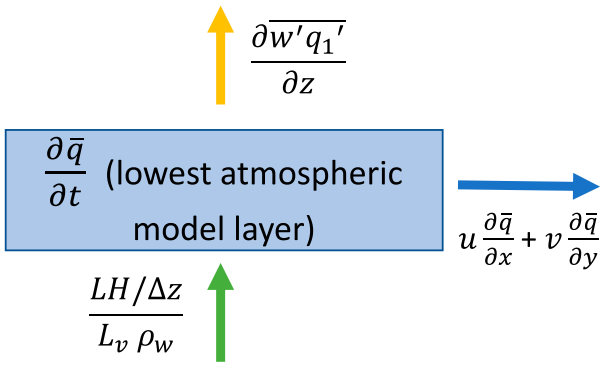

FIG. 1. Scheme illustrating the moisture budget of the model's lowest atmospheric layer. The direction of the arrow illustrates a positive contribution, so it will be the opposite direction when that item is negative. Evapotranspiration contributes to moisture increase, and it can be calculated from the latent heat flux (green arrow). The horizontal advection (blue arrow) is input through the forcing data, and the moisture exchange between this layer and the layer above (yellow arrow) is parameterized through the PBL scheme.

close to the observations, while the simulated wind speed profiles have larger differences. However, the simulated results capture the characteristics of the observed profiles during the evening transition, such as water vapor increase, stable boundary layer development, and low-level jet formation, albeit with differences in the timing, depth, and magnitude of these features.

b. *Near-surface processes*

Figure 3 shows time series of the different near-surface variables from the different cases, wherein the time axis is normalized to show the data relative to sunset (i.e., when the downwelling solar radiation reaches zero) for each case. The latent heat flux (Fig. 3a) decays gradually through the evening transition and is close to zero (but still slightly positive) after sunset. Although the magnitudes of the simulated and observed 2-m water vapor (Fig. 3b) are different, they both showed consistent increases during the transition. The simulated and observed net radiation matched very well (Fig. 3c), which was expected from the cloud-free conditions. The sensible heat flux (Fig. 3d) decays gradually and becomes negative about 2 h before sunset on 13 May, and it remains negative after that. Negative sensible heat flux means the surface is cooler than the air above, and heat is transported from the air to the surface. We question the reliability of the observed sensible heat fluxes from the ECOR on 15 and 16 May since they became negative around 1500 LT, which is not reasonable (the EBBR sensible fluxes were in better agreement, magnitude-wise, with the SCM results). On 13 May, sensible heat flux became negative around 1800 LT. Both the observed and simulated 2-m temperature (Fig. 3e) showed that there was an inflection point about 2 h before sunset. The temporal gradient of temperature was smaller before that point than after. Before sunset, 10-m wind speed also decreased (Fig. 3f). From these comparisons of near-surface variables, it can be seen that the model captured the evolution of the observations reasonably well.

c. *Moisture balance*

As we have mentioned in the section 3d, this study focuses on the near-surface water vapor increases during the evening transition, and the analysis of this study is the lowest atmospheric layer of the model. To investigate moisture balance of this layer, water-vapor-related and other closely related variables from the model are shown in Fig. 4. In the simulation, the physical height of the lowest atmospheric model layer was about 8–9 m above the ground surface, and its thickness was about 15 m. The temporal gradient of water vapor mixing ratio in this layer is given in Fig. 4a, and we can see the water vapor increase before sunset. Figure 4b is the turbulent kinetic energy (TKE) tendency due to buoyancy production or consumption. We can see that this term turned negative before sunset, coinciding with the time when the sensible heat flux becomes negative (Fig. 3d). Figure 4c is the vertical temperature gradient, which was calculated from the model skin temperature and the temperature of the first layer. A negative gradient means skin temperature is higher than the air temperature, while a positive gradient means skin temperature is cooler than the air temperature. Figure 4d is the specified horizontal advection of water vapor, which was calculated from RAP analysis data, and it is the advection term of Eq. (1). Figure 4d shows that the horizontal advection can be positive and negative around sunset (i.e., it does not seem to contribute consistently to the change in near-surface water vapor concentration). Figure 4e is the water vapor mixing ratio tendency due to inward turbulent flux from the surface into the lowest model layer, which was calculated from the latent heat flux of the model output. Figure 4f is the water vapor mixing ratio tendency due to outward turbulent flux from the lowest model layer to the adjacent layer above. Figures 4e and 4f together is the total water vapor mixing ratio tendency due to turbulence divergence/convergence, which is directly output from the CCPP SCM. Since the total water vapor mixing ratio tendency and the water vapor mixing ratio tendency due to inward turbulent flux are available, the water vapor mixing ratio tendency due to outward turbulent flux was calculated and is shown in Fig. 4f.

From these water-vapor-related and other closely related variables, we can see that the water vapor change in the lowest atmospheric model layer (Fig. 4a) was mainly caused by inward (i.e., evapotranspiration from the surface into the first atmospheric layer) and outward turbulent fluxes (i.e., from the first atmospheric layer to the second layer) (Figs. 4e,f, respectively), with the latter being responsible for the rapid changes in the water vapor gradient; the contribution of the horizontal advection was relatively small.

d. *Impact of horizontal advection and land cover*

To further investigate the impact of water vapor and temperature tendencies due to horizontal advection and land cover on the evening transition, three additional experiments were conducted. These experiments changed the magnitude of

Brought to you by NOAA Library | Unauthenticated | Downloaded 07/18/25 03:22 PM UTC

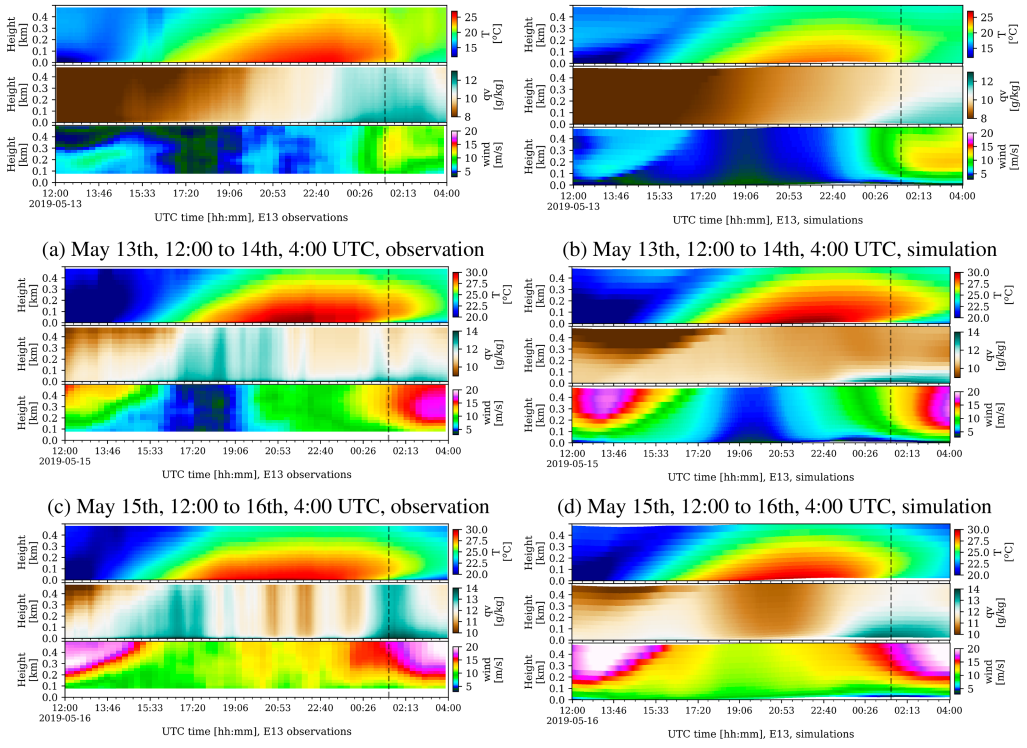

(a) May 13th, 12:00 to 14th, 4:00 UTC, observation

(b) May 13th, 12:00 to 14th, 4:00 UTC, simulation

(c) May 15th, 12:00 to 16th, 4:00 UTC, observation

(d) May 15th, 12:00 to 16th, 4:00 UTC, simulation

(e) May 16th, 12:00 to 17th, 4:00 UTC, observation

(f) May 16th, 12:00 to 17th, 4:00 UTC, simulation

FIG. 2. Time evolution of air temperature, water vapor mixing ratio, and wind speed profiles of the measurements and simulations for the different cases. The first column is for the measurements, and the second column is for the simulations. As noted in the horizontal axes, (top) 13 May 2019 case, (middle) 15 May 2019 case, and (bottom) 16 May 2019 case. The vertical dashed line in each plot represents the sunset time (i.e., when the downwelling solar flux reaches zero). Due to the properties of the DL, the wind speed can only be observed above 90 m AGL.

the tendencies of water vapor mixing ratio and potential temperature due to horizontal advection, reduced the amount of vegetation, and increased the amount of vegetation (Table 2). The control (ctrl) configuration had the same configuration as in the results discussed above. Experiment 1 (exp1) was designed to study the impact of horizontal water vapor and temperature advection on the results, and its advection was changed by multiplying two to the original values. Experiments 2 and 3 (exp2 and exp3, respectively) were designed to study the impact of land cover vegetation properties: exp2 is the scenario with sparse and unhealthy vegetation with a vegetation fraction of 0.1 and a leaf area index of 0.3, while exp3 is the scenario with dense vegetation with a vegetation fraction of 0.9 and a leaf area index of 4.

We conducted these experiments for all three cases (13, 15, and 16 May), and the results from the 3 days showed consistent results. The results of 16 May are presented here. Figure 5 shows the simulated near-surface variables from these different experiments. The results showed that doubling the horizontal advection impacted the pattern of the 2-m water vapor mixing ratio slightly, but the water vapor increase during the evening transition was still there (Fig. 5a). For the scenario of sparse vegetation (exp2), the near-surface variables were quite different from the control run. For example, its latent heat flux was much smaller than that of the ctrl, and its sensible heat flux was much larger than that of the ctrl. This was because vegetation transpiration was restrained when vegetation was sparse, and this led to the decrease of the 2-m water vapor. Since net radiation did not change, sensible heat flux increased to compensate for the decrease of latent heat flux. This led to the increase in the 2-m temperature. Wind speed increased slightly due to the sparse vegetation having a small roughness length. For the scenario of dense vegetation (exp3), these near-surface variables did not have a noticeable change compared to the default scenario. This happens because the simulated case was under water-limited transpiration, which means the availability of soil moisture determined how much water can be transpired but not the availability of energy.

The water-vapor-related variables during the evening transition for the control and experimental simulations are shown in Fig. 6. Figure 6a shows that water vapor increase started about 1.5 h later for the sparse vegetation scenario (exp2) relative to the other scenarios. Figure 6b shows that TKE tendency due to buoyancy production of the sparse vegetation (exp2) became negative later than the other scenarios. This is consistent with the time at which the vertical temperature gradient changed from negative to positive (Fig. 6c). Figure 6d shows that advection did change the magnitude of water vapor increase during

Brought to you by NOAA Library | Unauthenticated | Downloaded 07/18/25 03:22 PM UTC

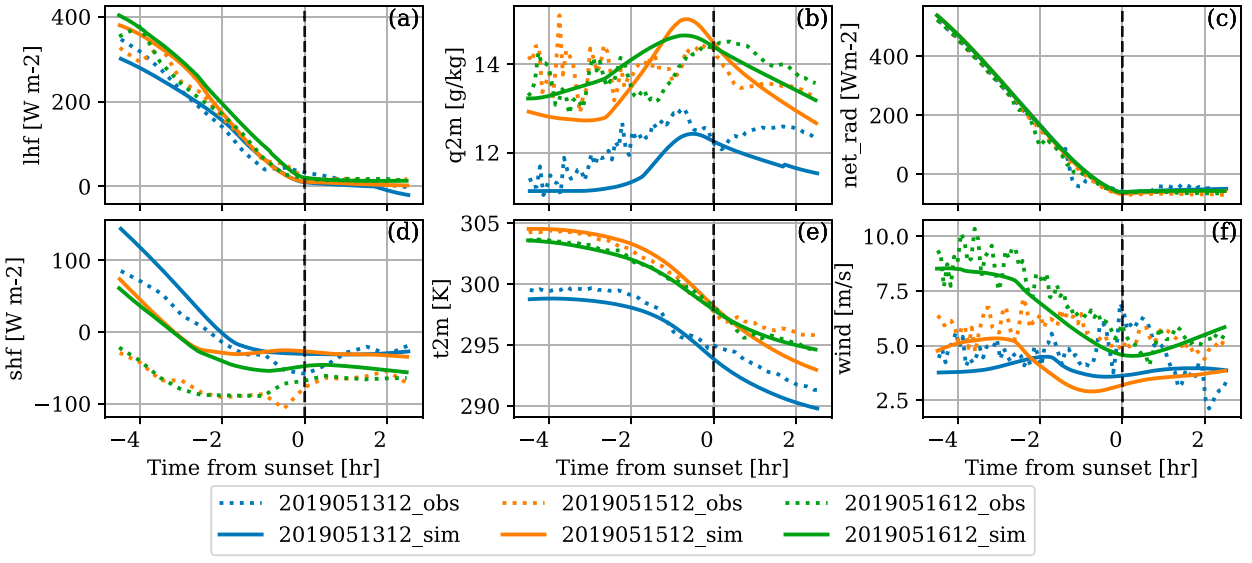

FIG. 3. Surface variables of the observations and simulations for the different cases. The *x* axis corresponds to time relative to sunset. (a) Latent heat flux, (b) 2-m water vapor mixing ratio, (c) net surface radiation, (d) sensible heat flux, (e) 2-m temperature, and (f) 10-m wind speed.

the evening transition, but the pattern of water vapor increase during the transition was still preserved. Figure 6e shows that the contribution of evapotranspiration to water vapor increase was smaller when the evapotranspiration was weaker (i.e., the sparse vegetation scenario). The turbulence term [the last term of Eq. (1)] does not produce water vapor, but it transports water vapor from one layer to another layer. Figure 6f shows that this term was smaller for the sparse vegetation scenario, which also has a smaller evapotranspiration.

6. Discussion

Four major findings of this study and their related mechanisms are discussed in this section.

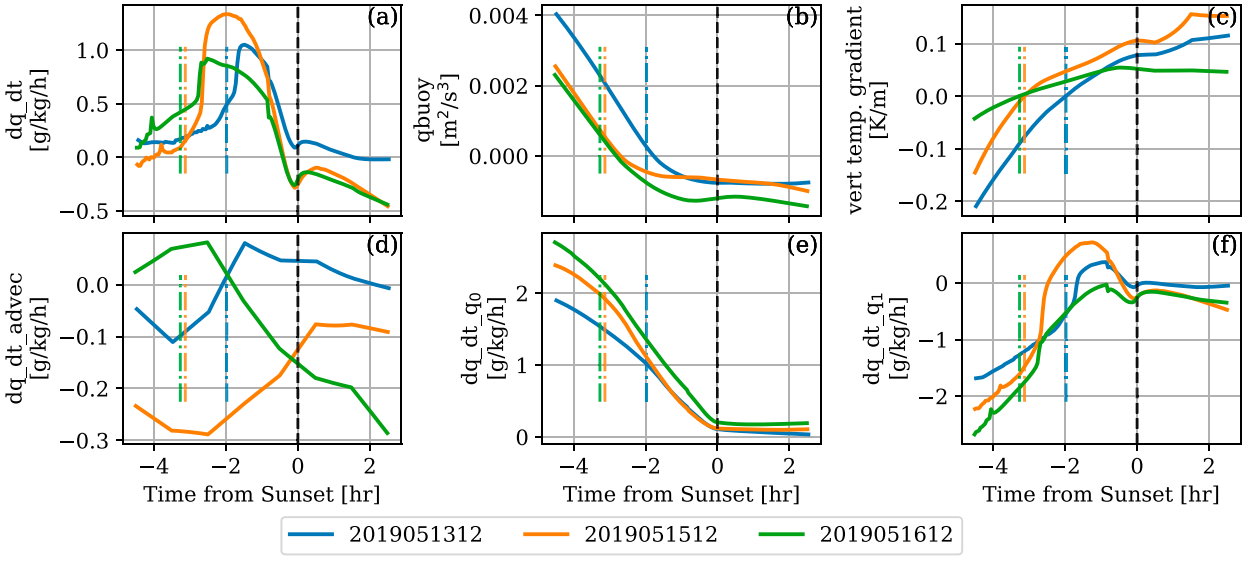

FIG. 4. Evolution of water-vapor-related and other closely related variables in the lowest atmospheric model layer (about 8 m above the surface). The *x* axis denotes time relative to sunset. In each subplot, the vertical dash–dotted line represents the time at which sensible heat flux changes from positive to negative. The panels show the model evolution of (a) total temporal gradient of water vapor mixing ratio, (b) TKE tendency due to buoyancy production, (c) vertical temperature gradient between the skin and the lowest atmospheric model layer, (d) horizontal advection of water vapor mixing ratio, (e) temporal gradient of water vapor mixing ratio due to inward turbulent flux (i.e., evapotranspiration from the surface into the first atmospheric layer), and (f) temporal gradient of water vapor mixing ratio due to outward turbulence flux (i.e., from the first atmospheric layer to the second layer).

Brought to you by NOAA Library | Unauthenticated | Downloaded 07/18/25 03:22 PM UTC

TABLE 2. Configurations for different SCM experiments.

Experiment	Scenario	Advection[a]	Vegetation fraction	LAI
ctrl	Default real	RAP	0.8	2.5
exp1	Strong advection	RAPx2	0.8	2.5
exp2	Sparse vegetation	RAP	0.1	0.3
exp3	Dense vegetation	RAP	0.9	4

[a]Including both moisture and temperature tendencies due to horizontal advection.

A critical time point in the evening transition is the time at which sensible heat flux changes its sign. Sensible heat, the transfer of heat between the surface and the atmosphere without any phase change, is dependent on the temperature difference between the surface and the overlying air, on turbulence, and on convection. Shortly after sunrise, the land surface becomes warmer than the overlying air and heat transfers from the surface to the atmosphere, which means the sensible heat flux is positive. Several hours before sunset (2–3 h in this study), the land surface becomes cooler than the overlying air due to the decrease of downwelling solar radiation. Thus, heat transfers from the atmosphere to the ground surface, which means the sensible heat flux is negative. In other words, the cooling of the surface relative to the overlying air led to the change of the sensible heat flux from positive to negative. Meanwhile, this cooling also led to the buoyant force changing sign (e.g., Figs. 4b and 6b). Buoyant force is a major component determining the magnitude of turbulence. From our experiments, we can see that the water vapor increases exactly happened when the sensible heat flux changed its sign, which means that the vertical temperature gradient is a trigger factor in the evening transition. The vertical temperature gradient change can be seen clearly from our results shown in Figs. 2, 4c, and 6c.

This study found that two processes, evapotranspiration and the evolution of the near-surface turbulent mixing, contribute to the near-surface water vapor increase during the evening transition period. Evapotranspiration is the main source of moisture that contributes to the near-surface water vapor increase, and when the atmosphere is unstable, this moisture is mixed over the deep convective boundary layer. However, when the sensible heat flux becomes negative, the atmosphere right next to the surface cools, creating a change in the vertical temperature gradient and hence a change in the sign of the buoyancy flux. Thus, the capability to transport water vapor from the first model layer to the adjacent layer through turbulence is decreased, and more water vapor stays in the first layer. This leads to the water vapor increase during the evening transition period. In other words, the increase in the water vapor from the surface (i.e., via evapotranspiration) is suddenly not being mixed efficiently into the layer above (i.e., the second atmospheric layer) during the evening transition, resulting in an increase in the water vapor mixing ratio in the first atmospheric layer. This is confirmed by the temporal shapes of the total temporal gradient of water vapor (Figs. 4a and 6a) and the temporal gradient of water vapor from turbulence (Figs. 4f and 6f).

As mentioned in the introduction, there are three associated hypotheses on the evening moisture increase. This study investigated these three factors. The results showed that evapotranspiration is the major source contributing to water vapor increase during the evening transition, but the timing of the rapid increase

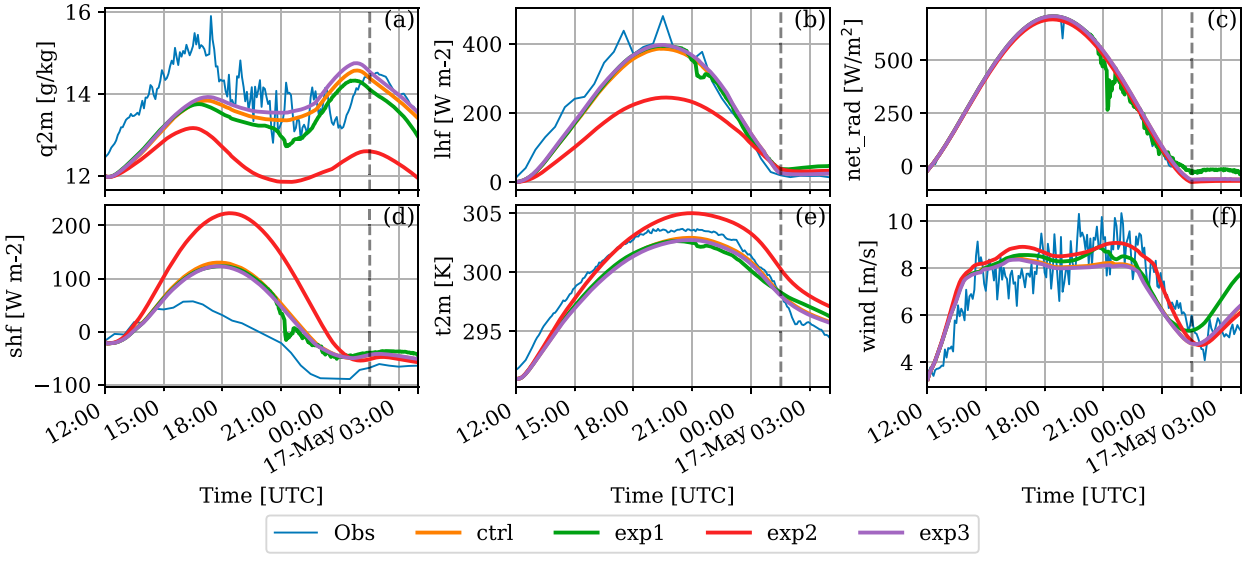

FIG. 5. Evolution of surface variables from observations and simulations for the 16 May case. The *x* axes are UTC time, and the dashed vertical line marks the sunset time. (a) The 2-m water vapor, (b) latent heat flux, (c) net surface radiation, (d) sensible heat flux, (e) 2-m temperature, and (f) 10-m wind speed.

Brought to you by NOAA Library | Unauthenticated | Downloaded 07/18/25 03:22 PM UTC

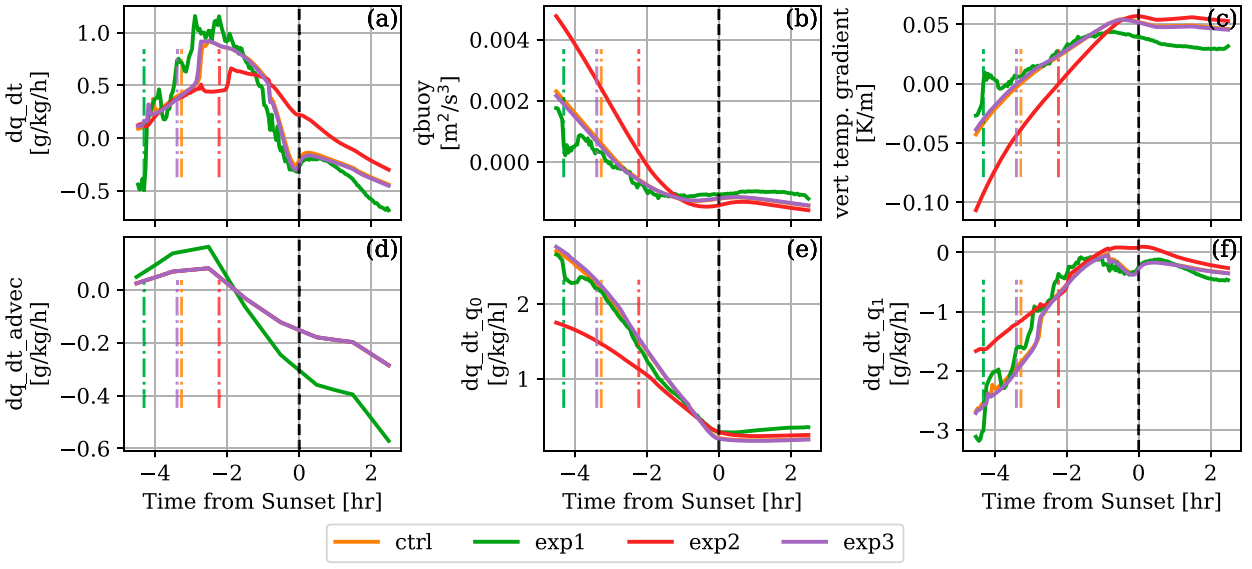

FIG. 6. As in Fig. 4, but for control and experimental SCM runs for the 16 May case. Evolution of water-vapor-related and other closely related variables in the lowest atmospheric model layer for control and experimental SCM runs for the 16 May case. The *x* axes are time offset from sunset. In each subplot, the vertical dash–dotted line represents the time at which sensible heat flux changes from positive to negative. (a) Total temporal gradient of water vapor mixing ratio, (b) TKE tendency due to buoyancy production, (c) vertical temperature gradient between the skin and the lowest atmospheric model layer, (d) horizontal advection of water vapor mixing ratio, (e) temporal gradient of water vapor mixing ratio due to inward turbulent flux, and (f) temporal gradient of water vapor mixing ratio due to outward turbulence flux.

in the near-surface water vapor concentration is controlled by the stability, and hence turbulent mixing, between the surface layer and the next adjacent layer. This is consistent with the conclusion from Acevedo and Fitzjarrald (2001). They found that the evening transition is dominated by vertical surface flux convergences as the turbulent mixing layer becomes confined to a shallow stable layer near the surface.

This study found that horizontal moisture advection can cause changes in the near-surface water vapor concentration. However, the role of horizontal advection to the near-surface water vapor change was variable during our three cases. Results of our three strong advection cases (only one case is shown in the figure) showed that horizontal advection can either lead to a water vapor increase or a water vapor decrease depending on the spatial water vapor gradients. In terms of the specific cases in this study, horizontal advection has no real role because (i) the surrounding land use is pasture and (ii) the Bowen ratio from the pasture and cropland is about the same during May 2019. Thus, there were no substantial secondary circulations that were formed. This has been investigated by Blumberg et al. (2019), showing that when the crops (wheat) are harvested but the adjacent pasture is still green, there can be large horizontal contrasts in the Bowen ratio, and secondary circulations could be formed in weak synoptic forcing conditions.

To verify that evapotranspiration is the main source causing water vapor increase from the long-term observations,

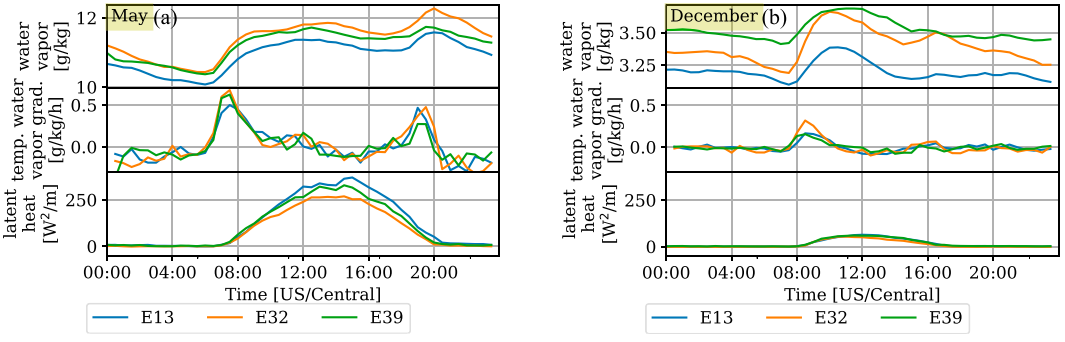

FIG. 7. Three-year diurnal averages of the (top) observed 2-m water vapor mixing ratio, (middle) temporal 2-m water vapor mixing ratio gradient, and (bottom) latent heat flux for (a) May and (b) December at three sites (i.e., E13, E32, and E39) of the SGP domain. The *x* axis is the time.

Brought to you by NOAA Library | Unauthenticated | Downloaded 07/18/25 03:22 PM UTC

we calculated the 3-yr diurnal averages of 2-m water vapor mixing ratio, temporal gradient of 2-m water vapor mixing ratio, and latent heat flux using in situ observations from three sites at the SGP domain. The results of May and December are given in Fig. 7. The results clearly show that water vapor increase during the evening transition was strong in May (Fig. 7a) but was hardly observable in December (Fig. 7b). Such a difference was caused by the difference of latent heat flux (i.e., evapotranspiration) in magnitude as showing in the bottom panels of Fig. 7. Thus, this supports the hypothesis that evapotranspiration is the main source causing water vapor increase.

Land cover impacts the magnitude of the near-surface water vapor increase, but it does not impact the trend of water vapor increase during the transition. We know that evapotranspiration is highly related to land cover, solar radiation, and soil conditions. In this study, scenarios of the dense and sparse vegetation were studied, respectively. Results showed that the dense vegetation scenario had much higher evapotranspiration than the sparse scenario, and this led to the magnitude of the near-surface water vapor being higher for the former than the latter. Another factor that is related to land cover is the time of sensible heat flux change signs. Evapotranspiration is the process of partitioning net radiation into sensible and latent heat fluxes. The dense vegetation scenario has a smaller Bowen ratio (ratio of sensible heat to latent heat) than sparse vegetation scenario, and water vapor increase during the evening transition tends to happen early. In this study, we found that water vapor increase for the dense vegetation (exp3) was about 1 h earlier than the sparse vegetation (exp2).

7. Conclusions

In this study, we used the CCPP SCM to study the near-surface water vapor increase during the evening transition. The main objectives are to investigate the sources causing this water vapor increase and to investigate the impacts of the land cover and horizontal advection on this water vapor increase. Several conclusions can be drawn through this study.

1) Changing the near-surface vertical temperature gradient from negative to positive, which is driven by the reversal of sign in the surface sensible heat flux, is the trigger of water vapor increase. This is because the near-surface turbulence divergence term decreases due to the buoyant force change caused by the temperature gradient change, and thus, less water vapor is mixed from the lower atmospheric layer into the ones above. A schematic plot illustrating the related processes and variables that contribute to an increase in near-surface moisture is provided in the supplement.
2) Evapotranspiration is the main source causing water vapor increase during the evening transition period, as the latent heat flux from the surface is still positive throughout the transition.
3) The impact of horizontal advection on water vapor varies from case to case, and it can either contribute to the water vapor increase or lead to a decrease in the water vapor depending on the spatial water vapor gradients.
4) Land cover impacts the timing of water vapor increase before sunset. Land cover with a small Bowen ratio tends to show water vapor increase earlier than land cover with a large Bowen ratio.

Acknowledgments. The authors also would like to thank Dr. Tilden Meyers of NOAA ARL, Dr. T. J. Wagner of the University of Wisconsin–Madison, and Drs. T. Heus and T. Rosenberger of the Cleveland State University for their helpful comments on this manuscript. Support for this analysis was provided via Grant 89243019SSC000034 provided by the DOE Atmospheric System Research (ASR) program and by the NOAA Atmospheric Science for Renewable Energy (ASRE) program. Stanley G. Benjamin, Julia M. Simonson, and Siwei He were supported during this work by NOAA Cooperative Agreement NA22OAR4320151. The authors also acknowledge the Developmental Testbed Center team for their development and maintenance of the CCPP SCM, as well as the editor and three reviewers for their insightful comments that significantly improved this manuscript.

Data availability statement. The in situ observed data of the SGP site are downloaded from the ARM web page (https://www.arm.gov/). The RAP data are available through Amazon Web Services (https://registry.opendata.aws/noaa-rap/). The simulated data of this manuscript can be accessed online (https://doi.org/10.5281/zenodo.10825849).

REFERENCES

Acevedo, O. C., and D. R. Fitzjarrald, 2001: The early evening surface-layer transition: Temporal and spatial variability. *J. Atmos. Sci.*, **58**, 2650–2667, https://doi.org/10.1175/1520-0469(2001)058<2650:TEESLT>2.0.CO;2.

Angevine, W. M., J. M. Edwards, M. Lothon, M. A. LeMone, and S. R. Osborne, 2020: Transition periods in the diurnally-varying atmospheric boundary layer over land. *Bound.-Layer Meteor.*, **177**, 205–223, https://doi.org/10.1007/s10546-020-00515-y.

Benjamin, S. G., and Coauthors, 2016: A North American hourly assimilation and model forecast cycle: The Rapid Refresh. *Mon. Wea. Rev.*, **144**, 1669–1694, https://doi.org/10.1175/MWR-D-15-0242.1.

Berg, L. K., L. D. Riihimaki, Y. Qian, H. Yan, and M. Huang, 2015: The low-level jet over the Southern Great Plains determined from observations and reanalyses and its impact on moisture transport. *J. Climate*, **28**, 6682–6706, https://doi.org/10.1175/JCLI-D-14-00719.1.

Bernardet, L., and Coauthors, 2024: Common community physics package: Fostering collaborative development in physical parameterizations and suites. *Bull. Amer. Meteor. Soc.*, **105**, E1490–E1505, https://doi.org/10.1175/BAMS-D-23-0227.1.

Blay-Carreras, E., E. R. Pardyjak, D. Pino, D. C. Alexander, F. Lohou, and M. Lothon, 2014: Countergradient heat flux observations during the evening transition period. *Atmos. Chem. Phys.*, **14**, 9077–9085, https://doi.org/10.5194/acp-14-9077-2014.

Blumberg, W. G., D. D. Turner, S. M. Cavallo, J. Gao, J. Basara, and A. Shapiro, 2019: An analysis of the processes affecting rapid near-surface water vapor increases during the afternoon

Brought to you by NOAA Library | Unauthenticated | Downloaded 07/18/25 03:22 PM UTC

to evening transition in Oklahoma. *J. Appl. Meteor. Climatol.*, **58**, 2217–2234, https://doi.org/10.1175/JAMC-D-19-0062.1.

Darbieu, C., and Coauthors, 2015: Turbulence vertical structure of the boundary layer during the afternoon transition. *Atmos. Chem. Phys.*, **15**, 10 071–10 086, https://doi.org/10.5194/acp-15-10071-2015.

Dowell, D. C., and Coauthors, 2022: The High-Resolution Rapid Refresh (HRRR): An hourly updating convection-allowing forecast model. Part I: Motivation and system description. *Wea. Forecasting*, **37**, 1371–1395, https://doi.org/10.1175/WAF-D-21-0151.1.

Edwards, J. M., R. J. Beare, and A. J. Lapworth, 2006: Simulation of the observed evening transition and nocturnal boundary layers: Single-column modelling. *Quart. J. Roy. Meteor. Soc.*, **132**, 61–80, https://doi.org/10.1256/qj.05.63.

Fang, H., F. Baret, S. Plummer, and G. Schaepman-Strub, 2019: An overview of global leaf area index (LAI): Methods, products, validation, and applications. *Rev. Geophys.*, **57**, 739–799, https://doi.org/10.1029/2018RG000608.

Firl, G., D. Swales, L. Carson, L. Bernardet, D. Heinzeller, and M. Harrold, 2022: Common community physics package single column model v6.0.0 user and technical guide. 45 pp., https://dtcenter.org/sites/default/files/paragraph/scm-ccpp-guide-v6-0-0.pdf.

Grant, A. L. M., 1997: An observational study of the evening transition boundary-layer. *Quart. J. Roy. Meteor. Soc.*, **123**, 657–677, https://doi.org/10.1256/smsqj.53906.

He, S., T. G. Smirnova, and S. G. Benjamin, 2021: Single-column validation of a snow subgrid parameterization in the Rapid Update Cycle land-surface model (RUC LSM). *Water Resour. Res.*, **57**, e2021WR029955, https://doi.org/10.1029/2021WR029955.

Iacono, M. J., J. S. Delamere, E. J. Mlawer, M. W. Shephard, S. A. Clough, and W. D. Collins, 2008: Radiative forcing by long-lived greenhouse gases: Calculations with the AER radiative transfer models. *J. Geophys. Res.*, **113**, D13103, https://doi.org/10.1029/2008JD009944.

Kim, Y.-J., and J. D. Doyle, 2005: Extension of an orographic-drag parametrization scheme to incorporate orographic anisotropy and flow blocking. *Quart. J. Roy. Meteor. Soc.*, **131**, 1893–1921, https://doi.org/10.1256/qj.04.160.

Knuteson, R. O., and Coauthors, 2004: Atmospheric emitted radiance interferometer. Part II: Instrument performance. *J. Atmos. Oceanic Technol.*, **21**, 1777–1789, https://doi.org/10.1175/JTECH-1663.1.

Koster, R. D., and Coauthors, 2004: Regions of strong coupling between soil moisture and precipitation. *Science*, **305**, 1138–1140, https://doi.org/10.1126/science.1100217.

Mahrt, L., 2000: Surface heterogeneity and vertical structure of the boundary layer. *Bound.-Layer Meteor.*, **96**, 33–62, https://doi.org/10.1023/A:1002482332477.

——, 2017: The near-surface evening transition. *Quart. J. Roy. Meteor. Soc.*, **143**, 2940–2948, https://doi.org/10.1002/qj.3153.

McCormack, J. P., S. D. Eckermann, D. E. Siskind, and T. J. McGee, 2006: CHEM2D-OPP: A new linearized gas-phase ozone photochemistry parameterization for high-altitude NWP and climate models. *Atmos. Chem. Phys.*, **6**, 4943–4972, https://doi.org/10.5194/acp-6-4943-2006.

——, K. W. Hoppel, and D. E. Siskind, 2008: Parameterization of middle atmospheric water vapor photochemistry for high-altitude NWP and data assimilation. *Atmos. Chem. Phys.*, **8**, 7519–7532, https://doi.org/10.5194/acp-8-7519-2008.

Olson, J. B., J. S. Kenyon, W. A. Angevine, J. M. Brown, M. Pagowski, and K. Sušelj, 2019: A description of the MYNN-EDMF scheme and the coupling to other components in WRF–ARW. NOAA Tech Memo. OAR GSD 61, 42 pp., https://doi.org/10.25923/n9wm-be49.

——, T. Smirnova, J. S. Kenyon, D. D. Turner, J. Brown, W. Zheng, and B. W. Green, 2021: A description of the MYNN surface layer scheme. NOAA Tech. Memo. OAR GSL-67, 26 pp., https://doi.org/10.25923/f6a8-bc75.

Pearson, G., F. Davies, and C. Collier, 2009: An analysis of the performance of the UFAM pulsed Doppler lidar for observing the boundary layer. *J. Atmos. Oceanic Technol.*, **26**, 240–250, https://doi.org/10.1175/2008JTECHA1128.1.

Santanello, J. A., and Coauthors, 2018: Land–atmosphere interactions: The LoCo perspective. *Bull. Amer. Meteor. Soc.*, **99**, 1253–1272, https://doi.org/10.1175/BAMS-D-17-0001.1.

Sisterson, D. L., R. A. Peppler, T. S. Cress, P. J. Lamb, and D. D. Turner, 2016: The ARM Southern Great Plains (SGP) site. The Atmospheric Radiation Measurement (ARM) Program: The First 20 Years, Meteor. Monogr., No. 57, Amer. Meteor. Soc., https://doi.org/10.1175/AMSMONOGRAPHS-D-16-0004.1.

Smirnova, T. G., and S. G. Benjamin, 2025: Advancements in the RUC land-surface model for use in the next-generation high-resolution weather prediction models. NOAA Tech. Memo. OAR GSL-73, 37 pp., https://doi.org/10.25923/55x8-cy36.

——, J. M. Brown, S. G. Benjamin, and J. S. Kenyon, 2016: Modifications to the Rapid Update Cycle land surface model (RUC LSM) available in the Weather Research and Forecasting (WRF) Model. *Mon. Wea. Rev.*, **144**, 1851–1865, https://doi.org/10.1175/MWR-D-15-0198.1.

Stull, R. B., 1988: *An Introduction to Boundary Layer Meteorology.* Springer Science and Business Media, 670 pp.

Thompson, G, and T. Eidhammer, 2014: A Study of Aerosol Impacts on Clouds and Precipitation Development in a Large Winter Cyclone. *Journal of the Atmospheric Sciences*, **71**, 3636–3658, https://doi.org/10.1175/JAS-D-13-0305.1.

Toy, M. D., J. B. Olson, F. Yang, B. Yang, and S.-Y. Hong, 2025: A description of the Unified Gravity Wave Physics package. OAR GSL-74, in press.

Turner, D. D., and U. Löhnert, 2014: Information content and uncertainties in thermodynamic profiles and liquid cloud properties retrieved from the ground-based Atmospheric Emitted Radiance Interferometer (AERI). *J. Appl. Meteor. Climatol.*, **53**, 752–771, https://doi.org/10.1175/JAMC-D-13-0126.1.

——, and W. G. Blumberg, 2019: Improvements to the AERIoe thermodynamic profile retrieval algorithm. *IEEE J. Sel. Top. Appl. Earth Obs. Remote Sens.*, **12**, 1339–1354, https://doi.org/10.1109/JSTARS.2018.2874968.

Turner, D. D., and R. G. Ellingson, 2016: Introduction. *The Atmospheric Radiation Measurement Program*, *Meteor. Monogr.*, No. **57**, v–x, https://doi.org/10.1175/AMSMONOGRAPHS-D-16-0001.1.

——, and U. Löhnert, 2021: Ground-based temperature and humidity profiling: Combining active and passive remote sensors. *Atmos. Meas. Tech.*, **14**, 3033–3048, https://doi.org/10.5194/amt-14-3033-2021.

van Heerwaarden, C. C., J. P. Mellado, and A. D. Lozar, 2014: Scaling laws for the heterogeneously heated free convective boundary layer. *J. Atmos. Sci.*, **71**, 3975–4000, https://doi.org/10.1175/JAS-D-13-0383.1.

Brought to you by NOAA Library | Unauthenticated | Downloaded 07/18/25 03:22 PM UTC

Wingo, S. M., and K. R. Knupp, 2015: Multi-platform observations characterizing the afternoon-to-evening transition of the planetary boundary layer in northern Alabama, USA. *Bound.-Layer Meteor.*, **155**, 29–53, https://doi.org/10.1007/s10546-014-9988-1.

Yang, F., H.-L. Pan, S. K. Krueger, S. Moorthi, and S. J. Lord, 2006: Evaluation of the NCEP Global Forecast System at the ARM SGP site. *Mon. Wea. Rev.*, **134**, 3668–3690, https://doi.org/10.1175/MWR3264.1.

Brought to you by NOAA Library | Unauthenticated | Downloaded 07/18/25 03:22 PM UTC